Assessment of intraoperative 3D imaging alternatives for IOERT dose estimation

Verónica García-Vázquez[1,*], Eugenio Marinetto[1], Pedro Guerra[2,3], Manlio Fabio Valdivieso-Casique[4], Felipe Ángel Calvo[1,5,6], Eduardo Alvarado-Vásquez[1,7], Claudio Vicente Sole[8,1], Kirby Gannett Vosburgh[9], Manuel Desco[10,1,11], Javier Pascau[10,1,11]

[1] Instituto de Investigación Sanitaria Gregorio Marañón, Madrid, Spain
[2] Departamento de Ingeniería Electrónica, ETSI Telecomunicación, Universidad Politécnica de Madrid, Madrid, Spain
[3] Centro de Investigación Biomédica en Red en Bioingeniería, Biomateriales y Nanomedicina (CIBER-BBN), Zaragoza, Spain
[4] GMV SA, Madrid, Spain
[5] Departamento de Oncología, Hospital General Universitario Gregorio Marañón, Madrid, Spain
[6] Facultad de Medicina, Universidad Complutense de Madrid, Madrid, Spain
[7] Servicio de Oncología Radioterápica, Hospital General Universitario Gregorio Marañón, Madrid, Spain
[8] Service of Radiation Oncology, Instituto de Radiomedicina, Santiago, Chile
[9] Department of Radiology, Brigham and Women's Hospital, Harvard Medical School, Boston, USA
[10] Departamento de Bioingeniería e Ingeniería Aeroespacial, Universidad Carlos III de Madrid, Madrid, Spain
[11] Centro de Investigación Biomédica en Red de Salud Mental (CIBERSAM), Madrid, Spain

Received 15 June 2016; accepted 19 July 2016

Abstract

Intraoperative electron radiation therapy (IOERT) involves irradiation of an unresected tumour or a post-resection tumour bed. The dose distribution is calculated from a preoperative computed tomography (CT) study acquired using a CT simulator. However, differences between the actual IOERT field and that calculated from the preoperative study arise as a result of patient position, surgical access, tumour resection and the IOERT set-up. Intraoperative CT imaging may then enable a more accurate estimation of dose distribution. In this study, we evaluated three kilovoltage (kV) CT scanners with the ability to acquire intraoperative images. Our findings indicate that current IOERT plans may be improved using data based on actual anatomical conditions during radiation. The systems studied were two portable systems ("O-arm", a cone-beam CT [CBCT] system, and "BodyTom", a multislice CT [MSCT] system) and one CBCT integrated in

Beurteilung der intraoperativen 3D-Bildgebungsalternativen für IOERT-Dosisabschätzung

Zusammenfassung

Die Intraoperative Elektronenstrahlentherapie (IOERT) beinhaltet die Bestrahlung eines inoperablen Tumors oder eines Tumorbetts nach der Resektion. Die Dosisverteilung wird aus einer präoperativen Computertomographie (CT)-Studie berechnet, für die ein CT-Simulator verwendet wurde. Resultierend aus der Patientenposition, dem chirurgischen Zugang, der Tumorresektion und dem IOERT-Aufbau tritt jedoch eine Abweichung zwischen dem tatsächlichen IOERT-Feld und dem aus der präoperativen Aufnahme berechneten Feld auf. Die Intraoperative CT-Bildgebung kann unter diesen Umständen eine genauere Einschätzung der

* Corresponding author: Verónica García-Vázquez, Instituto de Investigación Sanitaria Gregorio Marañón, Madrid, Spain.
E-mail: vgarcia@mce.hggm.es (V. García-Vázquez).

a conventional linear accelerator (LINAC) ("TrueBeam"). TrueBeam and BodyTom showed good results, as the gamma pass rates of their dose distributions compared to the gold standard (dose distributions calculated from images acquired with a CT simulator) were above 97% in most cases. The O-arm yielded a lower percentage of voxels fulfilling gamma criteria owing to its reduced field of view (which left it prone to truncation artefacts). Our results show that the images acquired using a portable CT or even a LINAC with on-board kV CBCT could be used to estimate the dose of IOERT and improve the possibility to evaluate and register the treatment administered to the patient.

Keywords: IOERT, radiotherapy, intraoperative imaging, dose distribution

Dosisverteilung ermöglichen. In dieser Studie haben wir drei Kilovolt (kV)-Computertomographgeräte bewertet, die intraoperative Bilder erstellen können. Unsere Ergebnisse weisen darauf hin, dass aktuelle IOERT-Behandlungspläne mittels Daten verbessert werden können, die auf tatsächlichen anatomischen Gegebenheiten während der Bestrahlung basieren. Es wurden zwei tragbare Systeme („O-Arm", ein cone-beam-CT [CBCT]-System und „BodyTom", ein Mehrschicht-CT [MSCT]-System) und ein in einen konventionellen Linearbeschleuniger integriertes CBCT-System (LINAC) namens „TrueBeam" untersucht. TrueBeam und BodyTom zeigten gute Ergebnisse, da die Gamma-Akzeptanzrate der Dosisverteilungen im Vergleich zum Goldstandard (Berechnung der Dosisverteilungen anhand von mit einem CT-Simulator aufgenommenen Bildern) in den meisten Fällen über 97% lag. Der O-Arm ergab einen niedrigeren Prozentsatz an Voxel, die die Gamma-Kriterien erfüllen. Dies liegt an seinem verminderten Sichtfeld, das seine Anfälligkeit für Truncation-Artefakte erhöht. Unsere Ergebnisse belegen die Verwendbarkeit von Bildern zur Einschätzung der IOERT-Dosis, die mit Hilfe eines tragbaren CT oder sogar eines LINAC mit On-Board-kV-CBCT erstellt wurden. Hierdurch können die Behandlungsdosen der Patienten besser bewertet und erfasst werden.

Schlüsselwörter: IOERT, Strahlentherapie, Intraoperative Bildgebung, Dosisverteilung

1 Introduction

Intraoperative electron radiation therapy (IOERT) involves irradiation of an unresected tumour or a post-resection tumour bed with a single-fraction, high-dose electron beam that is delivered by means of an applicator docked to a linear accelerator (LINAC) [1]. The displacement of non-involved organs and the use of shielding discs enable the dose administered to the target volume to be increased while diminishing the risk of irradiating healthy tissue.

A specific treatment planning system (TPS) was designed for IOERT procedures [2–4]. The dose distribution is calculated from a preoperative computed tomography (CT) study in which the position and orientation of the electron beam applicator is simulated virtually. This preoperative study is acquired with a CT simulator. Surgical access, tumour resection, organ displacement, bolus materials and shielding discs may also be incorporated in the simulation. The dose distribution is estimated by means of a pencil beam algorithm [5] or Monte Carlo algorithm [6] specifically adapted to this setting.

Patient position, surgical access, tumour resection and IOERT treatment set-up in the actual IOERT field can differ from those simulated in the TPS. Although acquiring a preoperative CT image of the patient in a position resembling the one used in the surgical procedure could reduce these differences, a better approach would be to use intraoperative CT imaging [7]. Relevant recent studies include that of [8], who proposed 2D portal imaging to ensure alignment between the applicator and the shielding disc in breast cancer IOERT. In [9], the authors conducted a preliminary phantom study to evaluate the feasibility of using a C-arm with 3D imaging capability (ARCADIS® Orbic 3D, Siemens, Germany) to acquire images during IOERT, concluding that C-arm image quality was a major limitation. In [10], the authors presented the first two clinical cases (Ewing sarcoma and undifferentiated sarcoma) in which intraoperative images were acquired using a CT simulator during IOERT. The patient was transferred from the operating room to the CT simulator room for acquiring an intraoperative CT image before the radiotherapy delivery in the treatment room. The 3D dose distribution of the actual treatment administered to the patient was calculated from the intraoperative CT image of the whole setting (patient and applicator) after superimposing the TPS virtual applicator on its actual position displayed in the CT image. Moreover, the dose was also estimated from their preoperative image after removing

the tumour and its surrounding area as expected during the surgery and then aligning to the intraoperative CT image using deformable registration. Despite that preprocessing, there were still differences between the dose distributions estimated with those preoperative images and those obtained from the intraoperative images (average difference of 5%). In [11] the authors pointed out that surface irregularities, simulated with a phantom, can significantly influence the IOERT dose distribution. Nowadays, IOERT is not entirely characterised since no intraoperative images of the actual scenario during the treatment are routinely acquired. This information would be useful not only for intraoperative planning but also for registering and evaluating the treatment administered to the patient. Following the approach of acquiring intraoperative images with CT simulators [10] has the limitation of the additional risks involved in transferring the patient to the CT simulator room, and this setup may not be justified if a dedicated mobile electron accelerator is available in the operating room.

In external beam radiation therapy (EBRT), imaging is currently used for identifying differences in patient positioning or target position prior to treatment delivery (image-guided setup correction). Many modern LINACs include integrated cone-beam CTs (CBCTs) that enable acquisition of 3D images with the patient in the treatment position that are then registered and compared with the planning CT. Moreover, these images can also be used to adapt the treatment plan depending on anatomical changes (weight loss, tumour regression and displacement) during the radiotherapy course [12]. Several articles have focused on the feasibility of using CBCT images for dose calculation in EBRT and show that CBCT images cannot be used directly for dose estimation because their quality is lower than that of CT simulator images. For instance, dose calculations for treatment fields that have a larger size and different geometry than the phantom used in the calibration procedure for converting CT values into density resulted in dose errors larger than 5% [13]. Several approaches have been proposed in order to overcome this problem, including mapping CT values from planning CT to CBCT after rigid alignment [14], treatment field-specific look-up tables that convert CT values to density [13], a density override method based on segmenting water, air and bone [15], and measuring the scatter distributions from the first CBCT scan acquired for patient setup and applying scatter correction on subsequent CBCT scans acquired throughout the radiotherapy course [16].

To our knowledge, no studies have evaluated the use of kilovoltage (kV) CT technologies other than CT simulators, as is the case of CBCT devices or even portable multislice CT (MSCT) scanners, to acquire intraoperative images for estimating IOERT dose distribution with the actual conditions. In this study, we evaluate the feasibility and potential of using kV CT imaging systems other than CT simulators that can be integrated in the IOERT workflow to calculate radiation doses more accurately.

2 Materials and methods

In this section, we describe the CT imaging systems evaluated in the study and the methodology followed to assess their potential. The devices were selected based on their suitability for imaging during IOERT. The three CT scanners chosen comprised two portable systems and one device integrated in a conventional LINAC. Two commercial phantoms were acquired using the systems under evaluation to simulate two representative IOERT treatments. The same phantoms were also imaged in a conventional CT simulator, and the dose distributions calculated from these studies formed the gold standards for our comparisons.

2.1 CT imaging systems evaluated

The three scanners with a kV CT imaging facility evaluated in this study were O-arm® Surgical Imaging (Medtronic, MN, USA), TrueBeam™ STx (Varian Medical Systems, CA, USA) and BodyTom® Portable CT Scanner (NeuroLogica Corporation, MA, USA) (Fig. 1).

Other commercial C-arms that provide 3D imaging capability include ARCADIS® Orbic 3D (Siemens, Germany), BV Pulsera (Philips, The Netherlands) and Ziehm Vision FD Vario 3D (Ziehm Imaging Inc., FL, USA). However, none of these devices was selected for this study owing to their reduced field of view (FOV).

The systems studied are described briefly below:

- O-arm is a portable kV cone-beam scanner with a large FOV and a sliding gantry that enables lateral access. It incorporates a 30 cm × 40 cm flat panel (Varian model PaxScan 4030 CB, amorphous silicon digital X-ray detector with a 1536 × 2048 pixel matrix and pixel pitch of 0.194 mm). The reconstructed FOV size is 20 cm (diameter) × 15 cm (height), with a matrix size of 512 × 512 × 192 and voxel size of 0.415 × 0.415 × 0.832 mm. O-arm has a gantry opening of 96.5 cm and its physical dimensions are 249 × 81.3 × 202.2 cm (length × width × height). It is mainly used in spinal and orthopaedic surgeries.
- TrueBeam combines the features of a LINAC and a kV CBCT. The on-board kV imager has a flat panel with a pixel matrix of 2048 × 1536 and an anti-scatter grid on top of the scintillator layer. The 3D image FOV is 46 × 46 × 16 cm for half-fan mode and 25 × 25 × 17 cm for full-fan mode, with a slice thickness ranging from 1 mm to 10 mm. The source-detector distance is 150 cm. Its imaging tools are used to verify the patient's position and tumour motion during treatment.
- BodyTom is a portable MSCT scanner (32 slices) with an FOV of 60 cm (slice thickness from 1.25 mm to 10 mm, image matrix 512 × 512). This CT device works in helical or axial mode and moves along the bed to perform acquisitions. BodyTom has a gantry opening of 85 cm and physical dimensions of 256.5 × 104 × 205.7 cm

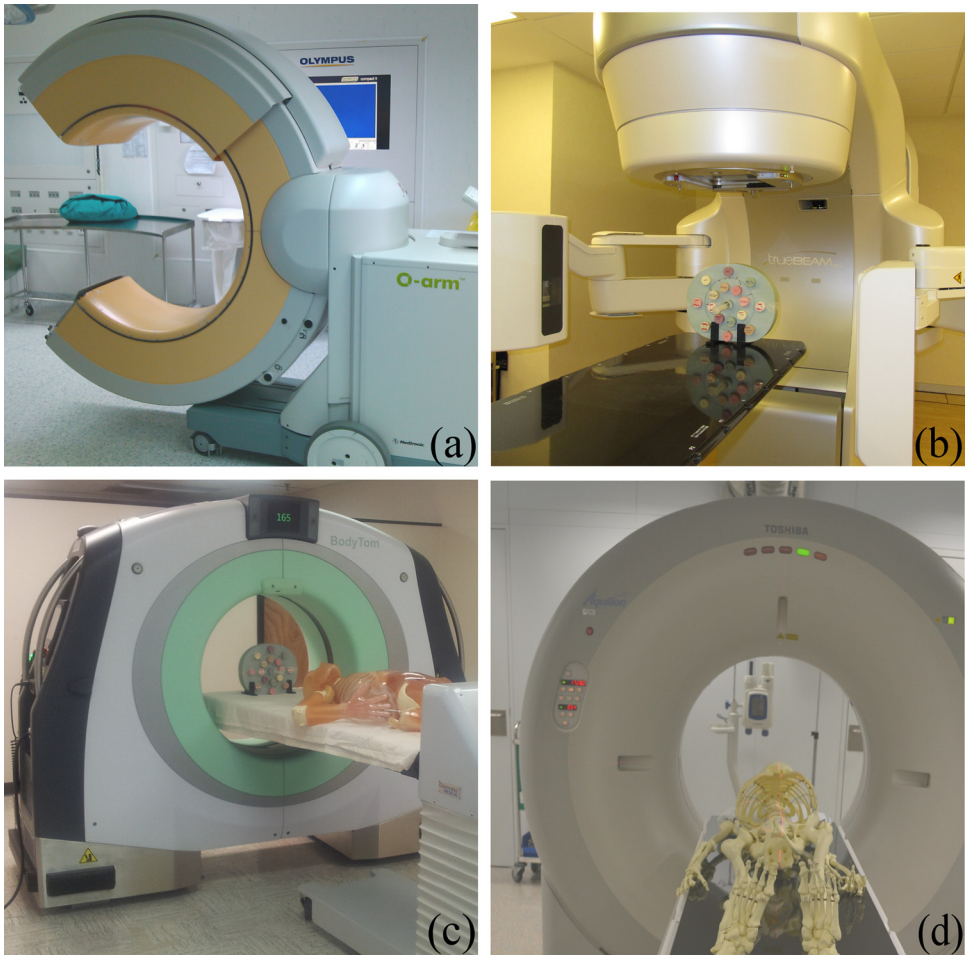

Fig. 1. CT scanners: (a) O-arm, (b) TrueBeam, (c) BodyTom, (d) CT simulator.

(length × width × height). The device is optimised for use in spinal surgery, tumour removal and interventional radiology.

All three devices fulfil the requirements for planning of radiotherapy using scanners with wide apertures (at least 70 cm [17]). Of the three, BodyTom has the smallest gantry opening. Wide apertures are essential in IOERT, since abdominal surgical retractors or patient position (e.g. lithotomy position) can prevent the patient from entering the gantry opening.

These devices could be a good solution for intraoperative imaging in IOERT procedures with different workflows. O-arm and BodyTom could be moved into the operating room in order to acquire the actual image before irradiating the patient with, for example, a mobile electron accelerator also located inside the operating room. TrueBeam, on the other hand, enables intraoperative images to be obtained before radiation is delivered with its conventional LINAC. Using the TrueBeam approach, it would be necessary to transfer the patient from the operating room to the LINAC room or alternatively the surgery could be performed in the LINAC facility, thus avoiding transportation.

2.2 CT simulator

The reference dose distributions were calculated from images acquired on an Aquilion™ Large Bore CT simulator (Toshiba, Japan). This multi-slice helical CT (16 slices) has a 70-cm FOV and a 90-cm gantry opening. This device is located in the Department of Radiation Oncology at Hospital General Universitario Marañón (Madrid, Spain) and its images are used for planning external radiotherapy treatments. This CT simulator fulfilled the image quality tests of the Spanish Society of Medical Physics (http://www.sefm.es; results: noise 0.4%, field uniformity 3.8 Hounsfield units [HU], CT number for air −980 HU and for water 3.8 HU [CT number accuracy], contrast resolution [low contrast resolution] 3.5% @ 2.5 mm and absence of artefacts) excepting the spatial resolution (high contrast resolution) test whose result (1 mm) was slightly higher than the manufacturer specification (0.6 mm). The spatial integrity [18] was

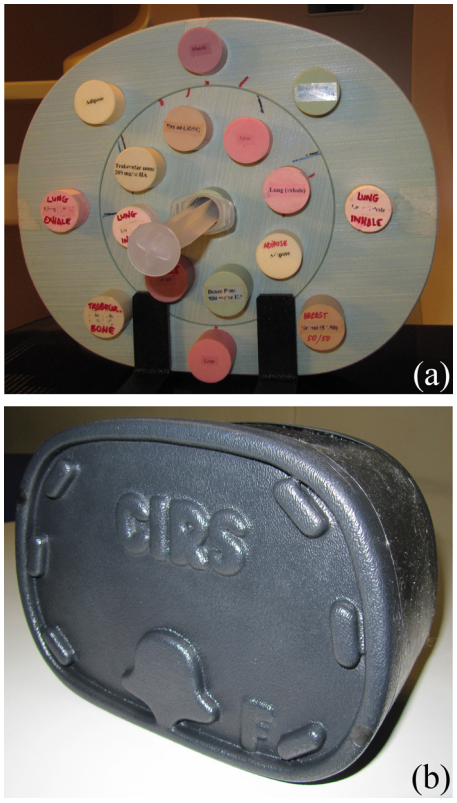

Fig. 2. Phantoms: (a) model 062 electron density phantom, (b) model 057 triple modality 3D abdominal phantom.

0.3 mm × 0.1 mm in the transaxial plane and 0.3 mm along the axial axis.

2.3 Phantoms

Two phantoms were used in this study: the model 062 electron density phantom and the model 057 triple modality 3D abdominal phantom, both from CIRS Inc. (VA, USA) (Fig. 2).

The model 062 phantom enables conversion from CT numbers to physical density to calibrate each scanner, since this relationship varies between scanners [19]. Conversion factors were incorporated into the IOERT TPS to take account of tissue heterogeneity in dose calculation. The phantom consists of two nested discs (a head insert and a body disc) made from Plastic Water® (dimensions 33 × 27 × 5 cm) and several plugs (dimensions: 30 mm diameter × 50 mm length) of eight different tissue equivalent epoxy resins (lung inhale, lung exhale, adipose, breast 50% gland/50% adipose, muscle, liver, trabecular bone 200 mg/cc hydroxyapatite [HA] and dense bone 800 mg/cc HA). A vial plug filled with sterilised water was placed at the centre of the phantom.

The model 057 phantom makes it possible to simulate a small adult abdomen approximately from thoracic vertebrae T9/T10 to lumbar vertebrae L2/L3 and includes the liver, part of both kidneys, part of the lung surrounding the liver, portal vein, vena cava, abdominal aorta, spine and six ribs. This phantom was used to simulate two IOERT cases in order to compare dose distributions calculated from images acquired with the devices evaluated and the CT simulator (gold standard). The phantom housing is made from acrylonitrile butadiene styrene (ABS) and the rest of the phantom from proprietary gels. Its dimensions are 28 × 20 × 12.5 cm.

2.4 CT acquisitions

Electron density and abdominal phantoms were scanned with each system. All CT acquisition parameters except matrix size were set to the same values for both phantoms in each scanner. Since the acquisition protocols offered a limited number of parameter combinations for each scanner, those selected were as similar as possible between scanners taking into account this restriction (Table 1). Tube voltage was selected according to typical CT protocols for radiotherapy planning.

2.5 Conversion of the CT number to physical density

Electron density phantom images were used to calibrate the conversion from CT numbers to physical density in each system. Cylindrical regions of interest (ROIs) of 20 mm diameter × 20 mm length were contoured centred on each plug, on the electron density head insert, on the electron density body disc, on the vial plug filled with sterilised water and outside the phantom (air). The ROI selected in the dense bone (800 mg/cc HA) equivalent electron density plug was smaller (6 mm diameter × 20 mm length) because the insert contains a 10-mm core of bone equivalent surrounded by water-equivalent material.

The electron density phantom is made of tissue-equivalent materials that represent the densities of tissues but do not usually replicate their chemical composition. These differences lead to large dose deviations (e.g. more than 30% for an 18-MeV electron beam [20]). To overcome this limitation, an in-house implementation of the stoichiometric calibration [21] was applied to obtain the CT numbers specific for each scanner of seven PENELOPE materials (dry air, lung, adipose tissue, striated muscle, muscle-equivalent liquid with sucrose, B100 and cortical bone) with known chemical composition and physical density. PENELOPE software is used to perform Monte Carlo simulation of coupled electron-photon transport and of electron and positron interactions [22]. The chemical composition of these PENELOPE materials closely follows the International Committee for Radiological Units (ICRU) or the International Commission on Radiological Protection (ICRP) standard chemical composition for biological tissues. B100 is a tissue substitute that has a chemical composition close to that of soft bone. The first step of the stoichiometric calibration was to find the two scanner-specific constants of the model that would fit the attenuation coefficient of a material relative to water. This model depends on the atomic number, the atomic weight, the percentage by weight of the

Table 1
CT acquisition parameters.

	Voltage (kV)	Exposure (mAs)	Matrix size	Voxel size (mm)
CT simulator	120	300	512 × 512 × 141[a] 512 × 512 × 251[b]	0.625 × 0.625 × 1
O-arm	120	298	512 × 512 × 192	0.415 × 0.415 × 0.832
TrueBeam (half-fan mode)	125	262	512 × 512 × 81	0.908 × 0.908 × 1.988
BodyTom (helical, soft tissue filter)	120	295	512 × 512 × 136[a] 512 × 512 × 128[b]	1.164 × 1.164 × 1.250

[a] Electron density phantom.
[b] Abdominal phantom.

different chemical elements that form that material and the physical density. Those constants, which are related to the cross-sections of photoelectric absorption, coherent scattering (Rayleigh) and incoherent scattering (Compton), were computed by a constrained least square fit of the CT numbers measured (i.e. the mean value for each ROI of the electron density phantom) to the aforementioned model, since CT numbers are related to attenuation coefficients relative to water. This estimation assumes that CT numbers are in HU so that X-ray attenuation of distilled water is defined as 0 HU and attenuation of air as −1000 HU at standard pressure and temperature. The chemical composition and physical density of the materials of the electron density phantom were provided by CIRS Inc. Once those constants were estimated, the CT number of each PENELOPE material was calculated by applying the fitted model. The CT numbers of those seven tissues and their physical density (calibration curve) were then entered into the IOERT TPS.

In the case of the O-arm scanner, two modifications to the procedure were necessary to convert the CT number to physical density. First, electron density phantom CT image values were linearly transformed, since the CT numbers for air and distilled water were different from −1000 HU and 0 HU, respectively. Second, as the FOV acquired by the O-arm covered only the electron density head insert, eleven ROIs were drawn on that image instead of the twenty ROIs segmented on the images from the other scanners. These adjustments were necessary to perform the stoichiometric calibration.

Several profiles were drawn on the electron density phantom images after rigid alignment of the studies from all the scanners (manual registration using the CT simulator image as a reference) in order to evaluate the variations in CT number within each plug between the CT simulator and each of the CT devices under evaluation.

2.6 Dose distribution evaluation

Two IOERT cases were simulated on the images from the abdominal phantom using the TPS *radiance* (GMV, Madrid, Spain) [4]: a pancreatic tumour and a soft-tissue sarcoma in paraspinal muscle. Abdominal images were resampled to 1.5-mm isotropic voxel size and then aligned (automatic rigid registration with normalised mutual information as cost function) using the CT simulator image as a reference. This procedure enabled us to place the IOERT applicator in the same position for all of the scanners. Dose distributions were calculated using the Monte Carlo algorithm (error tolerance 1%) [6], and doses were not scaled to a normalised value. The pencil beam algorithm was not used in this study, as it is subject to limitations with small irradiated volumes owing to the semi-infinite layer approximation and does not model backscatter radiation (e.g. that produced by shielding discs) [23].

In the case of the pancreatic tumour, the pancreas and liver were segmented and the CT numbers of the voxels inside those masks were set to air in order to simulate tumour resection and liver displacement, respectively. Surgical access was also simulated in the TPS. Tumour bed (clinical target volume [CTV]) and organs at risk (spinal cord, left kidney, aorta, and vena cava) were also contoured. The IOERT parameters were applicator diameter 50 mm, bevel angle 0°, energy 6 MeV and a prescribed dose of 15 Gy at a 90% isodose (Fig. 3(a)).

In the case of the paraspinal muscle sarcoma, the procedure followed was similar, namely, surgical access, tumour resection and segmentation of the CTV and organs at risk (spinal cord and right kidney). To protect the right kidney, two shielding discs were placed virtually between the CTV and the right kidney. A brass disc (thickness 3 mm, diameter 60 mm, physical density 8.6 g/cc) was placed close to the right kidney and a Tefal disc (thickness 3 mm, diameter 60 mm, physical density 2.2 g/cc) was positioned above the brass disc and towards the CTV to reduce backscattering radiation from the brass disc. The IOERT parameters were applicator diameter 50 mm, bevel angle 15°, energy 6 MeV and a prescribed dose of 12.5 Gy at a 90% isodose (Fig. 3(b)).

Dose distributions calculated from images obtained with the devices under evaluation were compared with the gold standard (CT simulator) in terms of the gamma index [24]. This measurement is the mainstay of dose distribution comparisons in medical physics and combines dose differences with the distance-to-agreement concept (DTA, distance between a point from the gold standard dose distribution and the nearest point in the evaluated dose distribution with the same dose as the reference data point). An acceptance criterion of 3% dose difference and a 3-mm DTA (3%/3 mm) for dose values greater than 10% is widely used in intensity-modulated radiation therapy [25]. However, since no values have been

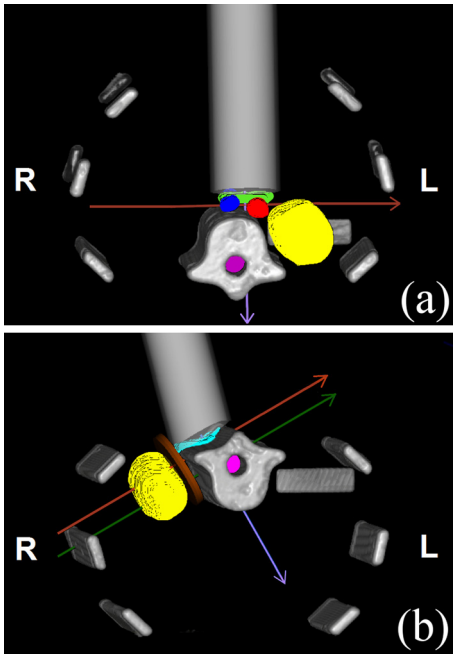

Fig. 3. Simulated IOERT cases: (a) pancreatic tumour (CTV in green, aorta in red, cava in blue, left kidney in yellow and spinal cord in purple), (b) paraspinal muscle sarcoma (CTV in blue, right kidney in yellow, spinal cord in purple and shielding discs in brown). Clinical axis in purple, transverse axis at depth of 10 mm in red and transverse axis at depth of 25 mm in green.

established for IOERT, we used a 3D gamma criteria of 3%/3 mm and 5%/2 mm for dose values greater than either 10% or 70% (to focus on high dose regions). The acceptance criterion 5%/2 mm includes a tighter distance tolerance that could be more appropriate for the characteristic dose distribution of electron beams (mainly dose decreases below 10% after only a few centimetres). Cumulative dose-volume histograms (DVHs), percentage of depth dose (PDD) profiles (along the clinical axis [perpendicular axis to the entry surface of the beam]) and transverse dose profiles (TDPs) at several depths were also obtained for both IOERT cases and all scanners (Fig. 3).

In the case of the O-arm scanner, the CT image of the abdominal phantom was first transformed by applying the same adjustment used with the electron density phantom in order to fix CT numbers.

3 Results

Fig. 4 illustrates the nonlinear CT to physical density conversions for all devices. The curves are similar until the inflection point at around 100 HU. For higher CT numbers, the physical density differs between scanners.

Fig. 5 shows three different profiles for each CT scanner, two on a transaxial view and one along the axial axis. O-arm intensity values presented an offset (corrected for

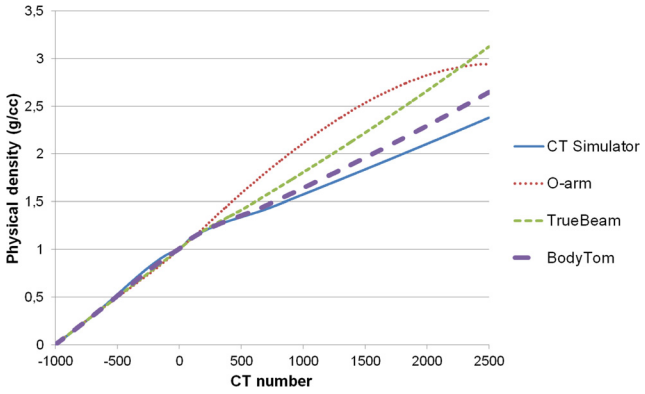

Fig. 4. Calibration curves for the transformation of CT numbers to physical density for each CT scanner.

stoichiometric calibration and dose estimation as explained in Materials and methods), and the intensity difference between materials was smaller than with the CT simulator. TrueBeam profiles were closer to the CT simulator profiles than those from the O-arm, although there was a smooth change in homogeneous areas such as Plastic Water (Fig. 5(a)) and incorrect CT values in trabecular bone (Fig. 5(b)). On the other hand, BodyTom CT numbers were quite similar to those of the CT simulator except for a disagreement in the dense bone values (Fig. 5(b)).

Two IOERT cases were simulated with the TPS using the images from the abdominal phantom. The registration results for all these CT images were checked by visual inspection. The FOV acquired by the O-arm did not cover the whole abdominal phantom, but the treatment volume and surrounding tissues were sufficiently covered to obtain comparable results. Figs. 6 and 7 show the dose distributions and the cumulative DVHs for both scenarios, respectively. In the case of the pancreatic tumour, the results for the different CT devices are quite close to the gold standard except for the O-arm, whose cumulative DVHs differ slightly from the reference. The DVHs of the left kidney and the spinal cord were not displayed since the 10% of the volume of those organs would receive a dose equal to or greater than 33 cGy in all devices. In the case of the paraspinal muscle sarcoma, the disagreement with the gold standard is slightly higher than in the case of the pancreatic tumour for all scanners, and is more noticeable in the spinal cord cumulative DVH calculated using the O-arm image. The DVH of the right kidney was not shown since the 10% of the volume of this organ would get a dose equal to or greater than 28 cGy in all devices. Fig. 8 shows the PDDs corresponding to both IOERT scenarios with the characteristic dose gradient of electron beams. The behaviour of the PDDs is similar to that of the DVHs. Dose differences with respect to the CT simulator increased with depth. On the other hand, the TDPs at 10 mm are similar to the CT simulator TDPs, except for the O-arm TDP from the case of the paraspinal muscle sarcoma (Fig. 9). Further analysis of this second IOERT case shows that the TDP at 25 mm went through the spinal cord, the

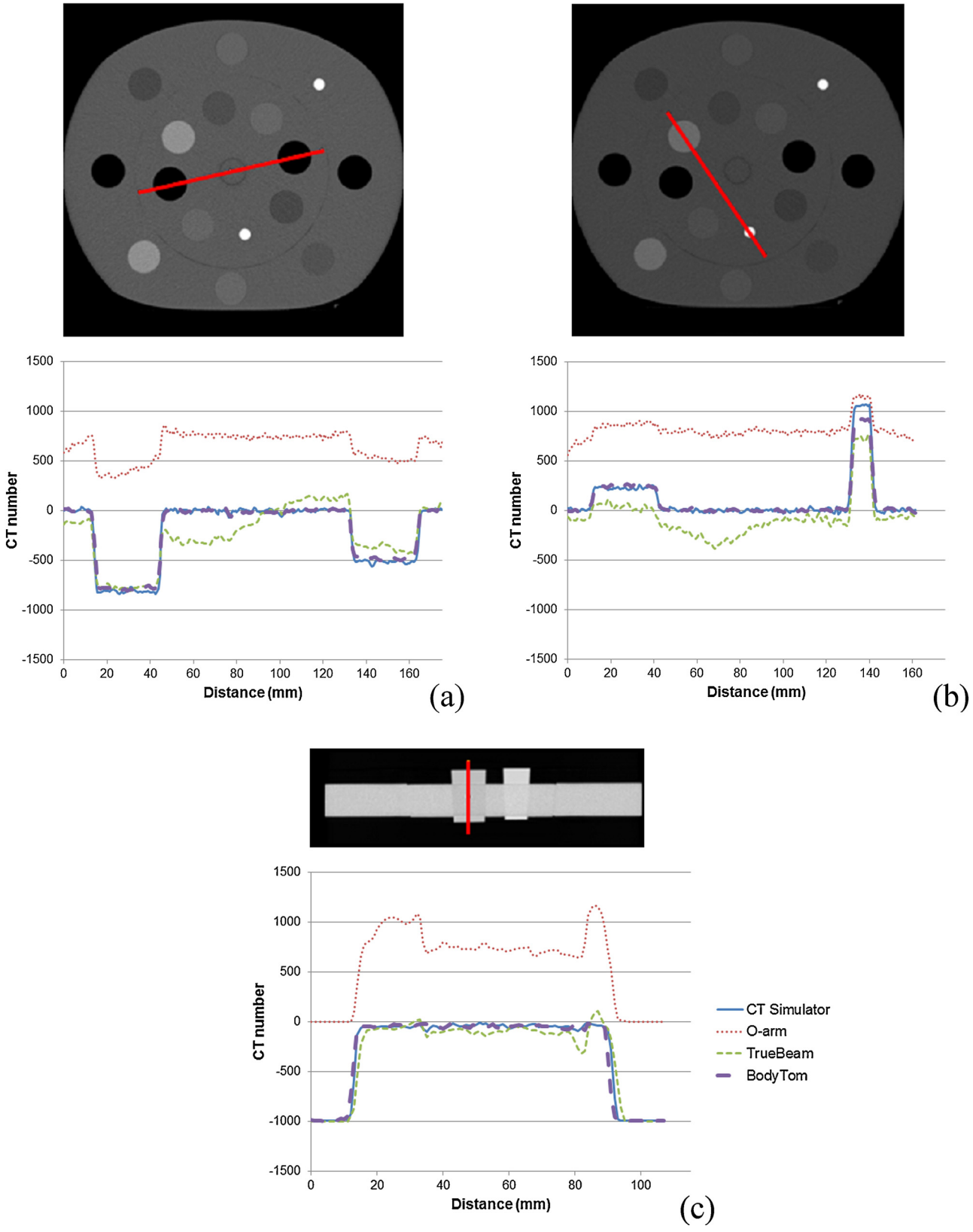

Fig. 5. Electron density phantom profiles for each CT scanner: (a) Lung inhale – Plastic Water – Lung exhale, (b) Trabecular bone 200 mg/cc – Plastic Water – Dense bone 800 mg/cc, (c) Air – Breast 50% gland/50% adipose – Air. Values shown for O-arm profiles are not corrected.

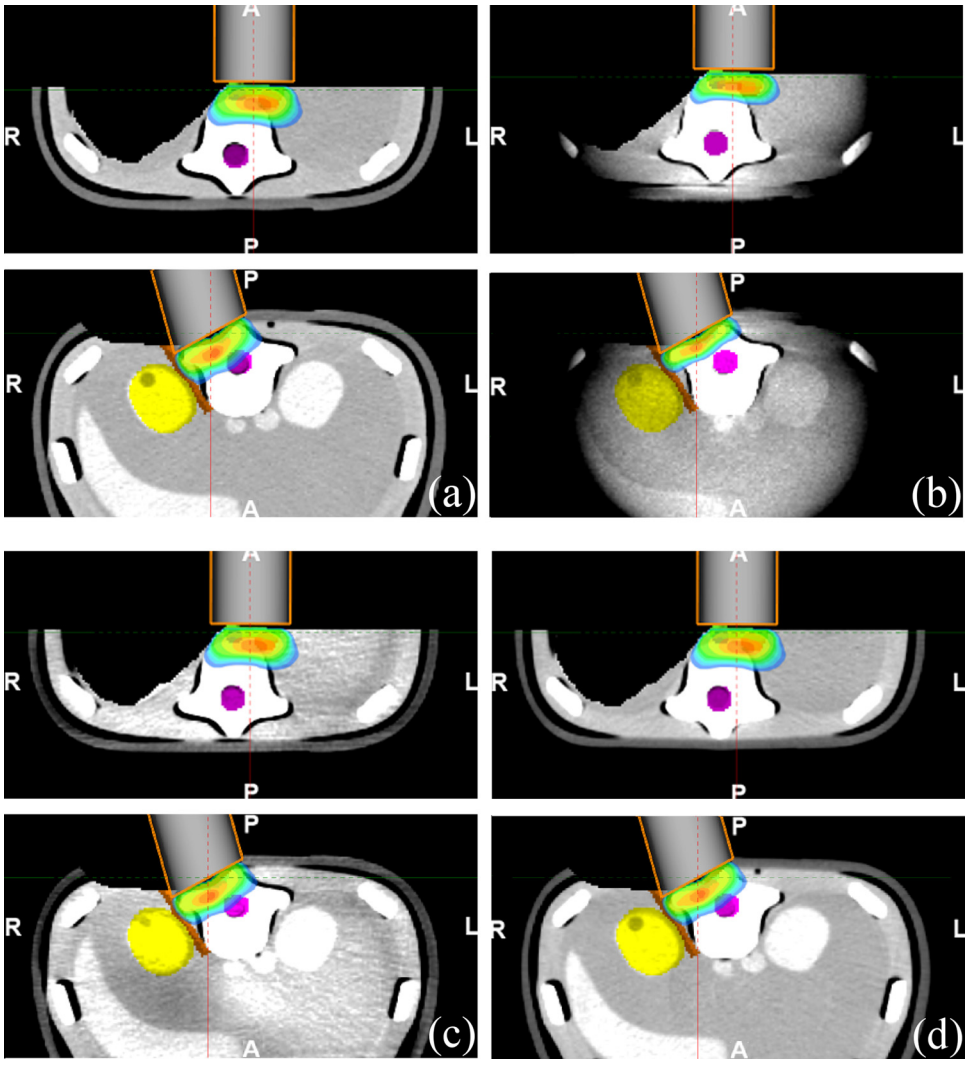

Fig. 6. Axial view of dose distributions. (a) CT simulator, (b) O-arm, (c) TrueBeam, (d) BodyTom. For every device, pancreatic tumour (top) and paraspinal muscle sarcoma (bottom). Spinal cord (purple), right kidney (yellow) and shielding discs (brown).

shielding discs and the right kidney (Fig. 9(c)). The percentage of dose is zero for the O-arm and higher for the TrueBeam and the BodyTom, but lower than the gold standard in all cases. Tables 2 and 3 include the percentage of voxels fulfilling selected gamma criteria (3%/3 mm and 5%/2 mm) for the pancreas and the paraspinal muscle respectively. Regarding the O-arm, the percentage is below 75% in both IOERT cases. TrueBeam showed values above 95% in all cases except in two comparisons, yielding gamma pass rates of 91.7% and 94.4% respectively in those specific scenarios (in the pancreatic

Table 2
Percentage of voxels fulfilling the gamma criteria for the case of the pancreatic tumour.[a]

	3%/3 mm		5%/2 mm	
	Dose > 10%	Dose > 70%	Dose > 10%	Dose > 70%
O-arm	52.3	70.8	45.9	68.7
TrueBeam	91.7	**97.9**	**95.9**	**99.7**
BodyTom	**100.0**	**100.0**	**100.0**	**100.0**

[a] Percentages of voxels fulfilling the gamma criteria higher than 95% are highlighted in bold.

Table 3
Percentage of voxels fulfilling the gamma criteria for the case of the paraspinal muscle sarcoma.[a]

	3%/3 mm		5%/2 mm	
	Dose > 10%	Dose > 70%	Dose > 10%	Dose > 70%
O-arm	43.3	55.6	37.4	47.8
TrueBeam	**98.1**	**97.7**	94.4	**97.0**
BodyTom	**98.7**	**99.9**	**99.1**	**100.0**

[a] Percentages of voxels fulfilling the gamma criteria higher than 95% are highlighted in bold.

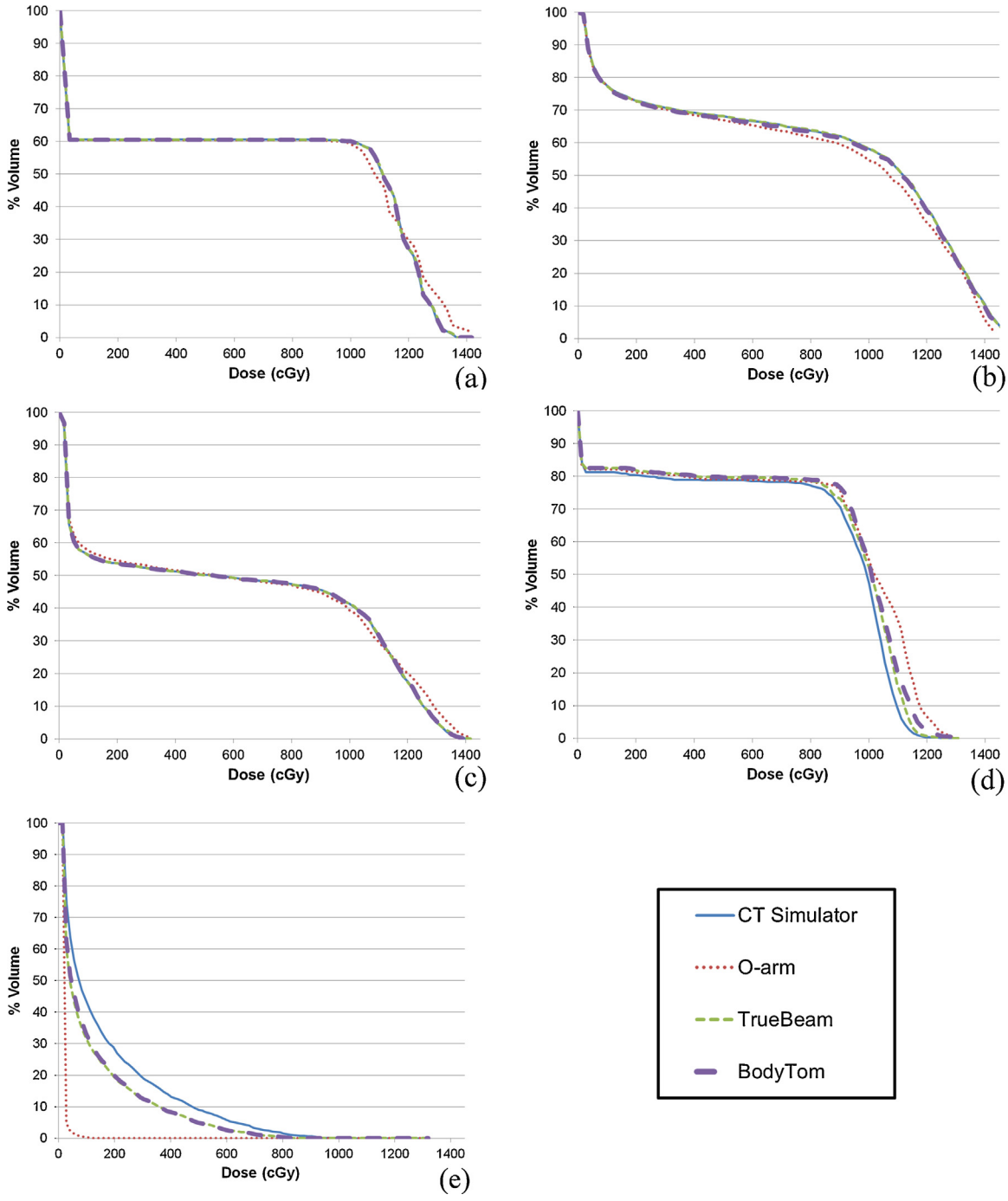

Fig. 7. Cumulative DVHs. In the case of pancreatic tumour, (a) tumour bed (CTV), (b) aorta, (c) cava. In the case of the paraspinal muscle, (d) CTV, (e) spinal cord.

tumour, when voxels with a dose higher than 10% and gamma criterion of 3%/3 mm were selected, and in the paraspinal muscle, when voxels with a dose higher than 10% and gamma criterion of 5%/2 mm were chosen). BodyTom yielded better results with more than 98% of voxels fulfilling the gamma criteria in all comparisons.

Finally, Table 4 shows the CT numbers of the seven PENELOPE materials obtained in the stoichiometric calibration and the CT numbers of several ROIs (circle of radius 3.5 mm) drawn in the abdominal phantom for each scanner. In the case of the O-arm, the CT numbers of the abdominal phantom do not follow the correspondence with those of PENELOPE

Table 4
CT numbers of the seven PENELOPE materials obtained in the stoichiometric calibration and CT numbers of several ROIs drawn in the abdominal phantom for each scanner.

		CT Simulator	O-arm (corrected values)	TrueBeam	BodyTom
PENELOPE materials	Dry air	−998.9	−998.9	−998.9	−998.9
	Lung	−701.7	−702.3	−701.6	−701.4
	Adipose tissue	−131.4	−72.3	−81.7	−102.2
	Striated muscle	32.4	32.8	34.6	34.5
	Muscle-equivalent liquid with sucrose	85.4	98.8	96.2	91.5
	B100	759.7	380.9	550.4	683.9
	Cortical bone	1526.2	741.5	1055.2	1331.0
Abdominal phantom	Soft tissue	43.6	376.0	66.5	43.7
	Liver	98.3	393.7	106.2	101.0
	Rib	495.6	499.5	477.0	471.9
	Vertebra	516.7	820.7	473.9	466.1

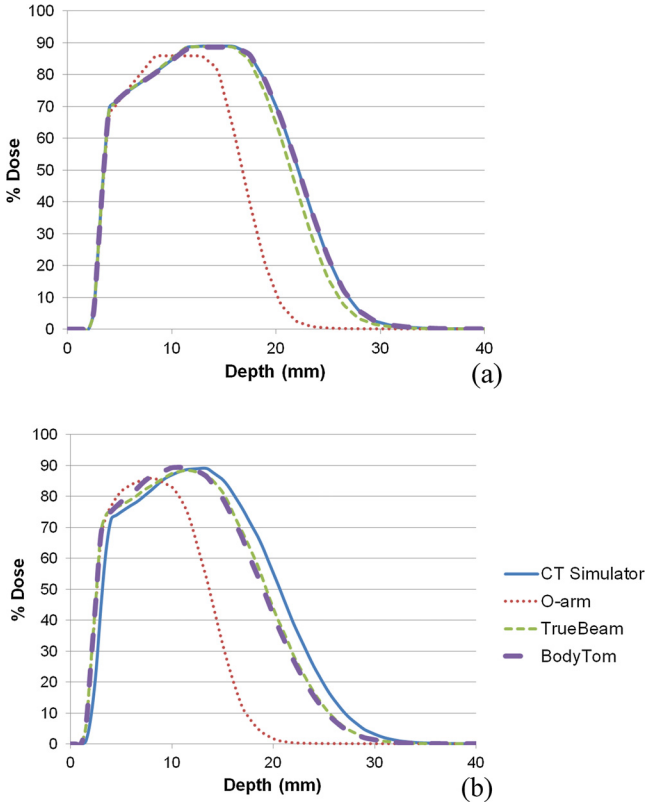

Fig. 8. PDDs in the case of the (a) pancreatic tumour and (b) paraspinal muscle sarcoma.

materials. For instance, the CT numbers of rib and vertebra ROIs should be below those of B100 for the O-arm device, as is the case for the CT simulator, TrueBeam and BodyTom.

4 Discussion

This is the first study to assess three kV CT imaging systems other than CT simulators with the ability to acquire intraoperative images in the IOERT framework. Since the evaluation focused on dose distribution rather than imaging performance for CT simulators, parameters such as image noise, spatial integrity, spatial resolution and contrast resolution [18] were not assessed.

TrueBeam and BodyTom showed very good agreement (BodyTom slightly better than TrueBeam) with the reference, with only small differences in terms of DVH, PDD, TDP at a specific depth and specific gamma criteria. This was not the case of the O-arm, which had a lower percentage of voxels fulfilling the gamma criteria. The main applications of O-arm device are spinal and orthopaedic surgeries, not the estimation of dose distributions. As for PDDs, differences were more noticeable at greater depths. This finding is consistent with previously published data for an energy level of 6 MeV [26]. Higher disagreement was observed for the case of the paraspinal muscle sarcoma (Fig. 9(c)): no dose is calculated for the O-arm and a lower value than the reference dose is calculated for the TrueBeam and BodyTom. As the spinal cord is centred at 25 mm, the underdosage in the PDDs (Fig. 8) and in the TDPs (Fig. 9(c)) led to underestimation of the spinal cord DVHs (Fig. 7). Nevertheless, that depth was out of the therapeutic range and close to the end of the practical range of all PDDs. The low dose in the spinal cord (paraspinal muscle sarcoma) with the O-arm was due to the wrong correspondence between the CT numbers of the abdominal phantom and those of the PENELOPE materials. In the case of the O-arm, CT numbers of the vertebra were higher than the values of the cortical bone. In the rest of devices, CT numbers of the vertebra were much lower than the values of the cortical bone. The number of electrons that would interact with the spinal cord would be lower in the case of the O-arm than in the rest of devices since physical densities assigned to the vertebra would be higher than the values for the cortical bone, thus reducing the dose in the spinal cord. The gamma criteria were only affected in the O-arm case.

Image artefacts are a major source of error when estimating dose distribution. They imply inconsistency between CT numbers in the reconstructed image and the true attenuation coefficients of the tissues. Two of the devices evaluated in this

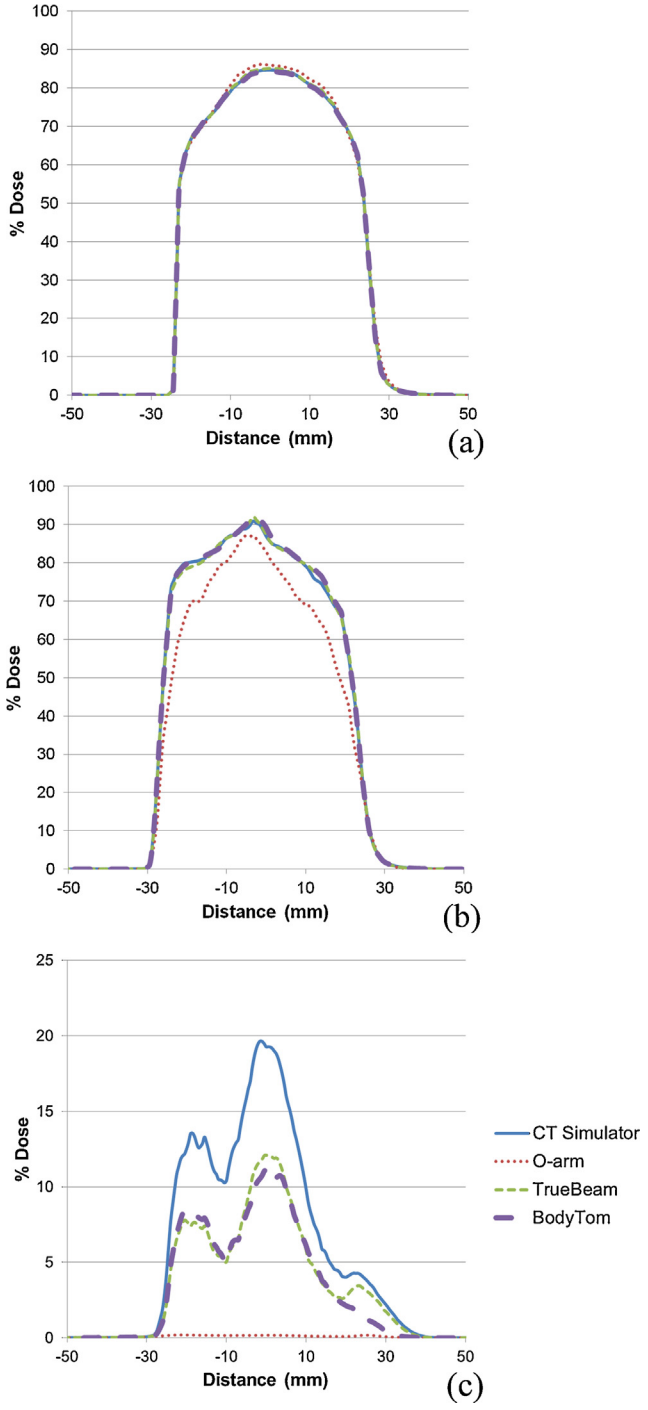

Fig. 9. TDPs at a depth of 10 mm in the case of the (a) pancreatic tumour and (b) paraspinal muscle sarcoma. TDPs at a depth of 25 mm in the case of the (c) paraspinal muscle sarcoma (shielding discs were at a position −30 mm).

study are CBCT systems. Although CBCT has a lower imaging dose than MSCT, it has disadvantages such as increased scattered radiation (increased noise, decreased contrast resolution, shadows, streaks and cupping artefacts), truncation artefacts (a rim of high-attenuation values combined with characteristic streaking), and movement artefacts; in addition, it does not provide actual HU [27,28]. Although [29] established a strong correlation between HU in MSCT and CT numbers in CBCT, their findings were based on the inaccurate assumption of a uniform relationship between X-ray attenuation and CT number through the CBCT image volume. Scattered radiation and beam hardening lead to CT number inhomogeneity [30]. On the other hand, since the electron density phantom and abdominal phantom differ in their dimensions and composition, scatter produced from both phantoms may affect CT numbers differently. In [31], the authors found that adding scatter longitudinally (by increasing phantom length) has a noticeable effect on CT number values (e.g. increasing up to approximately 260 HU in high-density materials when modifying phantom length from 5 cm to scan length [16 cm]), although this effect is much less profound than when adding radial scatter (by changing phantom diameter). Once the scan length was covered, the influence of the longitudinal scatter on CT numbers was reduced. These images were acquired using On-Board Imager^{TM} (OBI, Varian Medical Systems) version 1.4 (half-fan mode). In [32], the authors indicated that full scatter condition is necessary when obtaining the conversion from CT numbers to density for a CBCT (OBI, Varian Medical Systems) in order to have a better dose estimation using photon beams, especially in regions with large inhomogeneity. There is an extended version of the electron density phantom used in our study specifically designed for CBCTs (model 062MA). This phantom (dimensions 33 × 27 × 25 cm) contains other slabs of Plastic Water that allow full scatter of cone-beam X-ray. A stoichiometric calibration with this type of phantom together with a reconstruction method that included beam hardening and scatter corrections achieved a better CT number accuracy in CBCT images of head and neck phantoms using OBI version 1.4 (Varian Medical Systems) [33]. Our study did not include full scatter condition for the CBCTs devices (O-arm and TrueBeam). Nevertheless, TrueBeam results were good enough as the percentage of voxels fulfilling gamma criteria was above to 95% for most cases. In the case of the O-arm, acquiring the extended version of the electron density phantom would not fix its low gamma pass rates since it is not the main cause for that mismatch. Even after the CT number adjustment, O-arm values of analogous tissues in the electron density phantom and abdominal phantom images differ. This mismatch may be associated with the truncation artefact. Neither the electron density phantom (dimensions 33 × 27 × 5 cm) nor the abdominal phantom (28 × 20 × 12.5 cm) was completely scanned with the O-arm owing to its reduced FOV. CT reconstruction algorithms assume that the detector collects projection data for the whole object in all acquisition angles. Incomplete data from the object leads to truncation artefacts. In this situation, true linear attenuation coefficients cannot be calculated, and it is not possible to obtain actual HU [34]. In fact, CT numbers from CBCT images of the same object differ depending on the

FOV [35]. Any object that does not fit within the scanner FOV (large patients, retractors or the articulated arm that fixes the position of the applicator) can potentially generate truncation artefacts and thus lead to incorrect dose distributions.

While our analysis of imaging possibilities during IOERT is encouraging, several issues still need to be addressed. Firstly, reproducibility and long stability of the CT to physical density conversion for each evaluated device have not been assessed. In this study, images of the electron density phantom and the abdominal phantom were acquired with the same acquisition parameters (excepting matrix size) and within the same day for each evaluated device. This is important since tube voltage, collimation and filter type affect CT values (Synergy XVI, Elekta AB, Sweden) [13] while exposure has a small impact (Trilogy system, Varian Medical Systems) [36]. In [37], the authors pointed out that the stability of the calibration curve to transform CT numbers into density is system-dependent. For example, the X-ray Volume Imaging system mounted on a Elekta Synergy LINAC should be calibrated periodically because of a possible change in sensitivity of the flat panel detector (1-year evaluation period) [37]. On the other hand, the OBI calibration curve of the Varian Trilogy LINAC showed slight changes (6-month evaluation period) [38]. Recommendations from the Task Group 66 (TG-66, American Association of Physicists in Medicine, AAPM) establish that the CT number to density conversion should be evaluated at least annually or after a scanner calibration in the case of CT simulators [18]. Secondly, in the case of the pancreatic tumour, two shielding discs were virtually placed between the CTV and the right kidney. These protections would generate metal artefacts (severe streaking) that will substantially modify CT numbers, so the dose distribution estimated with intraoperative CT images of this IOERT scenario would be incorrect. Surgical retractors also produce this type of artefacts. Some ideas to get through this problem could be replacing the CT numbers that are affected by the metal artefact by their corresponding CT numbers in the preoperative images or, in the case of the retractors, removing these devices from the surgical scenario or replacing them with other surgical instruments that do not generate this artefact just before acquiring the intraoperative image. Despite these drawbacks, intraoperative images would provide useful information about the actual treatment field for radiation oncologists and medical physicists.

5 Conclusions

We assessed three kV CT imaging systems that can be used to acquire intraoperative images and thus update IOERT according to actual conditions. The evaluation was based on the comparison of dose distributions calculated with phantom images obtained for each of the CT devices under evaluation and for a CT simulator (gold standard). The results reveal that a portable CT (BodyTom) and even a LINAC with on-board kV CBCT (TrueBeam) would be suitable for this purpose. Owing to its reduced FOV (leading to truncation artefacts), the O-arm system produced the worst matching. Our results show the ability of the other two intraoperative imaging CT devices (TrueBeam and BodyTom) to estimate the IOERT dose. This information would be useful for intraoperative planning and for registering and evaluating the treatment administered to the patient.

Disclosure

Manlio F. Valdivieso-Casique works for GMV SA, which develops the IOERT TPS (*radiance*). Drs Felipe A. Calvo, Manuel Desco and Javier Pascau are co-inventors of the software *radiance* in a registered patent together with GMV. The authors declare that they have no conflicts of interest.

Acknowledgements

This study was supported by projects IPT-2012-0401-300000, TEC2013-48251-C2-1-R, DTS14/00192, PI-15/02121 (Ministerio de Economía y Competitividad, ISCIII), TOPUS-CM S2013/MIT-3024 (Comunidad de Madrid) and FEDER funds. We would like to acknowledge the support of the Madrid-MIT M+Vision Consortium in facilitating this study. KG Vosburgh received support from the National Center for Image Guided Therapy under NIH P41 EB015898. The authors also extend their gratitude to Medtronic, NeuroLogica Corporation, Department of Radiation Oncology at Clínica La Luz, Hospital Universitario La Paz, radiotherapy technicians at Hospital General Universitario Gregorio Marañón and Iván Balsa for their support with data acquisition. We are also grateful to the Department of Radiation Oncology at Hospital Universitario Ramón y Cajal for providing the electron density phantom, CIRS company for supplying the chemical composition of the phantom, Cristina González and Ramón Polo for providing image quality performance of the CT simulator, and Claudia de Molina and Alejandro Sisniega for technical assistance with CT artefacts. We would also like to express our sincere gratitude to the late Professor Juan Antonio Santos-Miranda for his practical and insightful suggestions regarding the task of improving IOERT procedures.

References

[1] Calvo FA, Meirino RM, Orecchia R. Intraoperative radiation therapy – First part: Rationale and techniques. Crit Rev Oncol Hematol 2006;59(2):106–15.

[2] Calvo FA, Sole CV, González ME, Tangco ED, López-Tarjuelo J, Koubychine I, et al. Research opportunities in intraoperative radiation therapy: the next decade 2013–2023. Clin Transl Oncol 2013;15(9):683–90.

[3] Pascau J, Santos Miranda JA, Calvo FA, Bouché A, Morillo V, González-San Segundo C, et al. An innovative tool for intraoperative electron beam radiotherapy simulation and planning: description and initial evaluation by radiation oncologists. Int J Radiat Oncol Biol Phys 2012;83(2):e287–95.

[4] Valdivieso-Casique MF, Rodríguez R, Rodríguez-Bescós S, Lardíes D, Guerra P, Ledesma MJ, et al. RADIANCE—a planning software for intra-operative radiation therapy. Transl Cancer Res 2015;4(2):196–209.
[5] Santos JA, Pascau J, Lardies MD, Desco M, Calvo F. Initial clinical experience of pencil beam dose modelling for intraoperative electron radiation therapy (IOERT). Radiother Oncol 2011;99(Supl. 1):S246.
[6] Guerra P, Udías José M, Herranz E, Santos-Miranda Juan A, Herraiz Joaquín L, Valdivieso Manlio F, et al. Feasibility assessment of the interactive use of a Monte Carlo algorithm in treatment planning for intraoperative electron radiation therapy. Phys Med Biol 2014;59(23):7159–79.
[7] García-Vázquez V, Marinetto E, Santos-Miranda JA, Calvo FA, Desco M, Pascau J. Feasibility of integrating a multi-camera optical tracking system in intra-operative electron radiation therapy scenarios. Phys Med Biol 2013;58(24):8769–82.
[8] Hanna SA, de Barros ACSD, de Andrade FEM, Bevilacqua JLB, Piato JRM, Pelosi EL, et al. Intraoperative radiation therapy in early breast cancer using a linear accelerator outside of the operative suite: an "image-guided" approach. Int J Radiat Oncol Biol Phys 2014;89(5):1015–23.
[9] Roeder F, Schramm O, Timke C, Habl G, Tanner MC, Huber PE, et al. Postplanning of a three-dimensional dose distribution for intraoperative electron radiation therapy (IOERT) using intraoperative C-arm based 3D-imaging – a phantom study. Int J CARS 2010;5(Suppl. 1):S71–2.
[10] Pascau J, Santos-Miranda J, González San-Segundo C, Illana C, Valdivieso M, García-Vazquez V, et al. Intraoperative imaging in IOERT sarcoma treatment: initial experience in two clinical cases. Int J Radiat Oncol Biol Phys 2011;81(2):S90.
[11] Costa F, Sarmento S, Sousa O. Assessment of clinically relevant dose distributions in pelvic IOERT using Gafchromic EBT3 films. Phys Med 2015;31(7):692–701.
[12] Srinivasan K, Mohammadi M, Shepherd J. Applications of linac-mounted kilovoltage cone-beam computed tomography in modern radiation therapy: a review. Pol J Radiol 2014;79:181–93.
[13] Richter A, Hu Q, Steglich D, Baier K, Wilbert J, Guckenberger M, et al. Investigation of the usability of conebeam CT data sets for dose calculation. Radiat Oncol 2008;3:42.
[14] van Zijtvetd M, Dirkx M, Heijmen B. Correction of conebeam CT values using a planning CT for derivation of the "dose of the day". Radiother Oncol 2007;85(2):195–200.
[15] Fotina I, Hopfgartner J, Stock M, Steininger T, Luetgendorf-Caucig C, Georg D. Feasibility of CBCT-based dose calculation: comparative analysis of HU adjustment techniques. Radiother Oncol 2012;104(2):249–56.
[16] Zhu L, Xie Y, Wang J, Xing L. Scatter correction for cone-beam CT in radiation therapy. Med Phys 2009;36(6):2258–68.
[17] Lecchi M, Fossati P, Elisei F, Orecchia R, Lucignani G. Current concepts on imaging in radiotherapy. Eur J Nucl Med Mol Imag 2008;35(4):821–37.
[18] Mutic S, Palta JR, Butker EK, Das IJ, Huq MS, Loo LND, et al. Quality assurance for computed-tomography simulators and the computed-tomography-simulation process: report of the AAPM radiation therapy committee task group no. 66. Med Phys 2003;30(10):2762–92.
[19] Constantinou C, Harrington JC, Dewerd LA. An electron-density calibration phantom for CT-based treatment planning computers. Med Phys 1992;19(2):325–7.
[20] Verhaegen F, Devic S. Sensitivity study for CT image use in Monte Carlo treatment planning. Phys Med Biol 2005;50(5):937–46.
[21] Schneider W, Bortfeld T, Schlegel W. Correlation between CT numbers and tissue parameters needed for Monte Carlo simulations of clinical dose distributions. Phys Med Biol 2000;45(2):459–78.
[22] Salvat F, Fernandez-Varea JM, Acosta E, Sempau J. PENELOPE, a code system for Monte Carlo simulation of electron and photon transport. In: Proceedings of a workshop/training course, OECD/NEA. 2011.
[23] Calama Santiago JA, Garcia-Romero A, Lardiés Fleta D, Infante Utrilla MA, Lopez Tarjuelo J, Ferrer Albiach C, et al. Pencil beam for electron intraoperative radiotherapy. Results of dose calculations in heterogeneous media. Radiother Oncol 2011;99(Suppl. 1):S13.
[24] Low DA, Harms WB, Mutic S, Purdy JA. A technique for the quantitative evaluation of dose distributions. Med Phys 1998;25(5):656–61.
[25] Ezzell GA, Burmeister JW, Dogan N, LoSasso TJ, Mechalakos JG, Mihailidis D, et al. IMRT commissioning: multiple institution planning and dosimetry comparisons, a report from AAPM Task Group 119. Med Phys 2009;36(11):5359–73.
[26] Nobah A, Moftah B, Tomic N, Devic S. Influence of electron density spatial distribution and X-ray beam quality during CT simulation on dose calculation accuracy. J Appl Clin Med Phys 2011;12(3):80–9.
[27] De Vos W, Casselman J, Swennen GRJ. Cone-beam computerized tomography (CBCT) imaging of the oral and maxillofacial region: a systematic review of the literature. Int J Oral Maxillofac Surg 2009;38(6):609–25.
[28] Strobel N, Meissner O, Boese J, Brunner T, Heigl B, Hoheisel M, et al. In: Reiser MF, Becker CR, Nikolaou K, Glazer G, editors. Multislice CT. Berlin/Heidelberg: Springer; 2009. p. 33–51.
[29] Mah P, Reeves TE, McDavid WD. Deriving hounsfield units using grey levels in cone beam computed tomography. Dentomaxillofac Radiol 2010;39(6):323–35.
[30] Oliveira ML, Tosoni GM, Lindsey DH, Mendoza K, Tetradis S, Mallya SM. Influence of anatomical location on CT numbers in cone beam computed tomography. Oral Surg Oral Med Oral Pathol Oral Radiol 2013;115(4):558–64.
[31] Hatton J, McCurdy B, Greer PB. Cone beam computerized tomography: the effect of calibration of the hounsfield unit number to electron density on dose calculation accuracy for adaptive radiation therapy. Phys Med Biol 2009;54(15):N329–46.
[32] Ahn BS, Wu H-G, Yoo SH, Park JM. Improvement of dose calculation accuracy on kV CBCT images with corrected electron density to CT number curve. J Radiat Prot Res 2015;40(1):17–24.
[33] Elstrøm UV, Olsen SRK, Muren LP, Petersen JBB, Grau C. The impact of CBCT reconstruction and calibration for radiotherapy planning in the head and neck region – a phantom study. Acta Oncol 2014;53(8):1114–24.
[34] Jaju PP, Jain M, Singh A, Gupta A. Artefacts in cone beam CT. Open J Stomatol 2013;3:292–7.
[35] Parsa A, Ibrahim N, Hassan B, Motroni A, van der Stelt P, Wismeijer D. Influence of cone beam CT scanning parameters on grey value measurements at an implant site. Dentomaxillofac Radiol 2013;42(3):79884780.
[36] Rong Y, Smilowitz J, Tewatia D, Tome WA, Paliwal B. Dose calculation on kV cone beam CT images: an investigation of the HU-density conversion stability and dose accuracy using the site-specific calibration. Med Dosim 2010;35(3):195–207.
[37] Takemura A, Tanabe S, Tokai M, Ueda S, Noto K, Isomura N, et al. Long-term stability of the Hounsfield unit to electron density calibration curve in cone-beam computed tomography images for adaptive radiotherapy treatment planning. J Radiother Pract 2015;14(4):410–7.
[38] Yadav P, Ramasubramanian V, Paliwal BR. Feasibility study on effect and stability of adaptive radiotherapy on kilovoltage cone beam CT. Radiol Oncol 2011;45(3):220–6.